coatings

MDPI

Article

Hot Corrosion Behavior of $BaLa_2Ti_3O_{10}$ Thermal Barrier Ceramics in V_2O_5 and Na_2SO_4 + V_2O_5 Molten Salts

Hui Liu [1,*], Jin Cai [2] and Jihong Zhu [1]

[1] School of Mechanical Engineering, Northwestern Polytechnical University, Xi'an 710072, China; Jh.zhu_fea@nwpu.edu.cn

[2] College of Aerospace Engineering, Shenyang Aerospace University, Shenyang 110136, China; saucai@sau.edu.cn

* Correspondence: cr_si@nwpu.edu.cn; Tel.: +86-24-2438-2359; Fax: +86-24-2432-6643

Received: 12 March 2019; Accepted: 10 April 2019; Published: 29 May 2019

Abstract: $BaLa_2Ti_3O_{10}$ ceramics for thermal barrier coating (TBC) applications were fabricated, and exposed to V_2O_5 and Na_2SO_4 + V_2O_5 molten salts at 900 °C to investigate the hot corrosion behavior. After 4 h corrosion tests, the main reaction products resulting from V_2O_5 salt corrosion were $LaVO_4$, TiO_2, and $Ba_3V_4O_{13}$, whereas those due to Na_2SO_4 + V_2O_5 corrosion consisted of $LaVO_4$, TiO_2, $BaSO_4$ and some $Ba_3V_4O_{13}$. The structures of reaction layers on the surfaces depended on the corrosion medium. In V_2O_5 salt, the layer was dense and had a thickness of 8–10 μm. While in Na_2SO_4 + V_2O_5 salt, it had a ~15 μm porous structure and a dense, thin band at the bottom. Beneath the dense layer or the band, no obvious molten salt was found. The mechanisms by which the reaction layer forms were discussed.

Keywords: thermal barrier coating (TBC); $BaLa_2Ti_3O_{10}$; molten salt corrosion; corrosion mechanisms

1. Introduction

Thermal barrier coatings (TBCs) are extensively used in turbine engines, which can protect engine hot-components against thermal attack and corrosion, giving rise to enhanced engine efficiencies and performances [1–3]. Usually, a typical TBC system is composed of a ceramic topcoat and a metallic bond coat [4–6]. The top coat is important, which provides thermal insulation to the substrate, and is commonly made of yttria partially stabilized zirconia (YSZ) [1,2,7–9]. Up to now, many techniques have been developed to produce YSZ coatings [10–13].

In a marine environment or engines use low-quality fuel, molten salts have severe damage to YSZ TBCs, especially at a temperature range of 600–1000 °C [14–18]. Molten salts infiltrate into the TBCs, and react with YSZ grains to form YVO_4, leading to the depletion of yttria stabilizer in the TBC. During engine heating-cooling cycles, phase transformation of the TBC occurs, causing the coating to spall much faster than if no molten salt exists. Many researchers have studied the corrosion mechanisms of YSZ TBCs resulting from molten salt [18–22]. Some strategies have been proposed to improve the hot corrosion resistance of YSZ coatings, such as doping CeO_2, Al_2O_3, Ta_2O_5 and RE_2O_3 (RE = rare earth element) into the system [18,21–24].

Increasing engines operating temperature leads to enhanced power output and efficiency [1–3]. However, YSZ TBCs suffer from phase transformation and reduced thermal insulation above 1200 °C, which causes them unlikely to meet the long-term requirements for advanced engines. Moreover, even lower thermal conductivity of TBCs is practically required for better thermal insulation. Therefore, alternative TBC materials to YSZ suitable for high-temperature applications are strongly needed. For

the application at higher temperatures, a similar threat to new TBCs posed by molten salts still exists. Thus, there is a strong need to understand the hot corrosion behavior of TBC candidates in molten slats.

Recently, the hot corrosion behavior of some newly developed TBC materials in molten salts has been reported. Ouyang et al. have studied the hot corrosion behavior of $Gd_2Zr_2O_7$ and $Yb_2Zr_2O_7$ ceramics in V_2O_5 molten salt at various temperatures [16,25]. Cao et al. have investigated the corrosion products of $LaTi_2Al_9O_{19}$ ceramic resulted from V_2O_5 salt attack, and proposed their formation mechanisms [17]. Recently, Guo et al. have systematically studied the hot corrosion behavior and mechanisms of some TBC candidates in molten salts, such as Ba_2YbAlO_5, $(Gd_{0.9}Sc_{0.1})_2Zr_2O_7$, Gd_2O_3-Yb_2O_3 co-doped YSZ and rare earth phosphate [26–29]. They reported that these novel TBC materials reveal better corrosion resistance than YSZ. Specially, $LaPO_4$ and $NdPO_4$ are found to highly resist to molten salt corrosion; exposed to high temperatures, the molten salt reacts with the ceramics to form an RE(P,V)O_4 (RE = Nd, La) solid solution, which leads to limited damage to the original microstructure [29]. $BaLa_2Ti_3O_{10}$ has been considered as a promising TBC candidate material [30], however, how it behaves in molten salts is not found in the open literature.

In order to understand the corrosion resistance of $BaLa_2Ti_3O_{10}$, its hot corrosion behavior in V_2O_5 and Na_2SO_4 + V_2O_5 salts for 4 h at 900 °C is investigated. In this study, the emphasis is placed on analyzing the corrosion products resulting from the reactions between $BaLa_2Ti_3O_{10}$ and the molten salts by using dense pellets, and the associated corrosion mechanisms are also discussed.

2. Experimental Procedures

$BaLa_2Ti_3O_{10}$ powders were produced by a solid-state reaction method. The raw materials contained $BaCO_3$, TiO_2 and La_2O_3 powders, which were dissolved in ionized water in an appropriate quantity. Then, the powders were ball mixed using zirconia media at a speed of 400 rpm for 10 h, followed by drying at 160 °C for 10 h. Afterward, the mixed powders were calcined at 1500 °C for 24 h. The bulk samples for hot corrosion tests were fabricated from the powders, which were cold pressed at ~250 MPa and then sintered at 1500 °C for 10 h.

The corrosion media were V_2O_5 and 50 mol% Na_2SO_4 + 50 mol% V_2O_5 (Na_2SO_4 + V_2O_5) salts. Prior to hot corrosion tests, pellets were ground by 800 grit sandpaper. Then, the samples were ultrasonic cleaned in ethanol and dried at 120 °C. The salts were uniformly spread on surfaces of samples, and its content was determined by weighting the samples before and after the salt coverage using an analytical balance. The salt concentration was ~10 mg/cm^2. Then, the salt covered samples were heated at 900 °C for 4 h in a furnace, followed by cooling in the furnace.

Phase structures of the corroded samples was identified by X-ray diffraction (XRD; Rigaku Diffractometer, Tokyo, Japan), with 2θ range of 10°–80° at a scanning rate of 0.1°/s. Surface morphologies were obtained by SEM (TDCLS4800, Hitachi Ltd., Tokyo, Japan), the composition analysis was performed using EDS (IE 350), and cross-sectional images were taken by SEM (TDCLSU1510, Hitachi Ltd.).

3. Results and Discussion

Figure 1 shows the XRD patterns of the as-prepared $BaLa_2Ti_3O_{10}$ pellet and the samples after hot corrosion. $BaLa_2Ti_3O_{10}$ bulk basically consists of a monoclinic phase. It is possible to observe that the peaks are sharp, suggesting good crystallization of the sample. After V_2O_5 salt corrosion, $LaVO_4$ (PDF#50-0367), $Ba_3V_4O_{13}$ (PDF#36-1466) and TiO_2 (PDF#99-0090) phases are detected by XRD on the sample surface. In the case of Na_2SO_4 + V_2O_5 salt corrosion, the corrosion products are $LaVO_4$, $Ba_3V_4O_{13}$, TiO_2 and $BaSO_4$, and some $BaLa_2Ti_3O_{10}$ diffraction peaks are also detected, as indicated in Figure 1. The corrosion products resulting from the two type of slats are different, which will be further confirmed by SEM and EDS analysis in the following section.

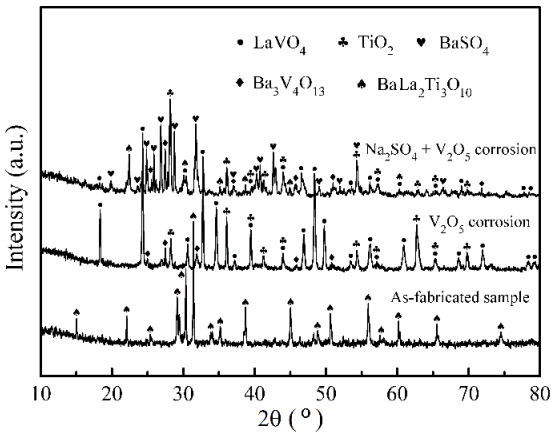

Figure 1. XRD patterns of $BaLa_2Ti_3O_{10}$ powders and the samples after hot corrosion in V_2O_5 and $Na_2SO_4 + V_2O_5$ salts at 900 °C for 4 h.

Figure 2a shows the surface image of the as-fabricated $BaLa_2Ti_3O_{10}$ pellet. Obvious $BaLa_2Ti_3O_{10}$ grains are observed. After hot corrosion in V_2O_5 salt, corrosion products are observed on the sample surface, as can be seen in Figure 2b. When observing the corrosion products at a higher magnification, one could find three different shapes, i.e., plate-shaped (marked as A), rod-shaped (marked as B) and particle-shaped (marked as C), as shown in Figure 2c. EDS analysis result listed in Table 1 indicates that A consists of Ba, V and O elements. In combination with the above XRD result, it is possible to determine that A is $Ba_3V_4O_{13}$. B is composed of Ti and O, and C contains La, V and O. Further analysis confirms that B and C are TiO_2 and $LaVO_4$, respectively.

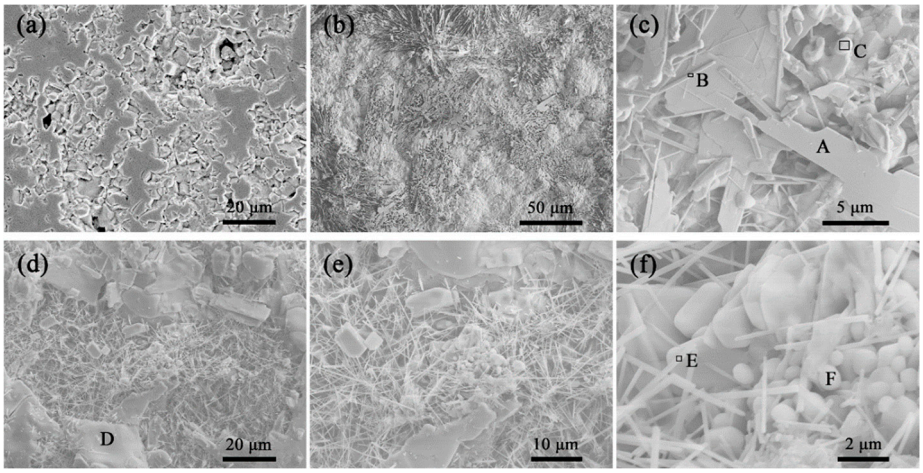

Figure 2. Surface morphologies of the as-fabricated $BaLa_2Ti_3O_{10}$ pellet (**a**), and the samples after V_2O_5 corrosion (**b**,**c**) and $Na_2SO_4 + V_2O_5$ corrosion (**d**–**f**).

Table 1. Compositions of compounds A–F in Figure 2 (in at.%).

Corrosion Products	Ba	La	Ti	V	S	O
A	15.87	–	–	21.56	–	62.57
B	–	–	31.58	–	–	68.42
C	–	16.38	–	17.63	–	65.99
D	16.45	–	–	–	18.53	65.02
E	–	–	33.16	–	–	66.84
F	–	17.57	–	18.46	–	63.97

After hot corrosion in Na_2SO_4 + V_2O_5 salt, the pellet surface is also completely covered with corrosion products, as shown in Figure 2d. The plate-shaped compounds (D) have Ba, S and O elements, without any evidence of V, as shown in Table 1, and they could be identified to be $BaSO_4$. Enlarging the image of the surface, one could find many rod-shaped and particle-shaped compounds, as presented in Figure 2e. These two different shaped compounds are marked as E and F, respectively in Figure 2f. As listed in Table 1, compound E contains Ti and O, and F has La, V and O, which could be confirmed to be TiO_2 and $LaVO_4$, respectively.

Figure 3a shows the cross-sectional image of the $BaLa_2Ti_3O_{10}$ sample after hot corrosion in V_2O_5 salt at 900 °C for 4 h. A continuous, dense reaction layer forms on the sample surface. Beneath the layer, the bulk keeps structure integrity, where no molten salt trace could be observed. This indicates that this layer has a positive function on suppressing the molten salt penetration. In the enlarged image (Figure 3b), it is possible to find that the layer is highly adhered to the bulk, with a thickness of 8–10 μm. Note that there are two sub-layers in the reaction layer. The upper sub-layer is light-contrasted and has some cracks, while the lower sub-layer is grey-contrasted and reveals a dense structure. EDS analysis was conducted on regions A–C in Figure 3c, and the results are presented in Table 2. The elements in Regions A and B are identical, including La, Ti, Ba, V and O. In combination with the above XRD result and the surface SEM analysis, it could be confirmed that the two sub-layers are composed of $Ba_3V_4O_{13}$, $LaVO_4$ and TiO_2. The different contrast of the two sub-layers might be attributed to the difference in the $Ba_3V_4O_{13}$ content. In region C, Ba, La, Ti and O elements are detected, with no evidence of V, implying that it has not been attacked by V_2O_5 molten salt.

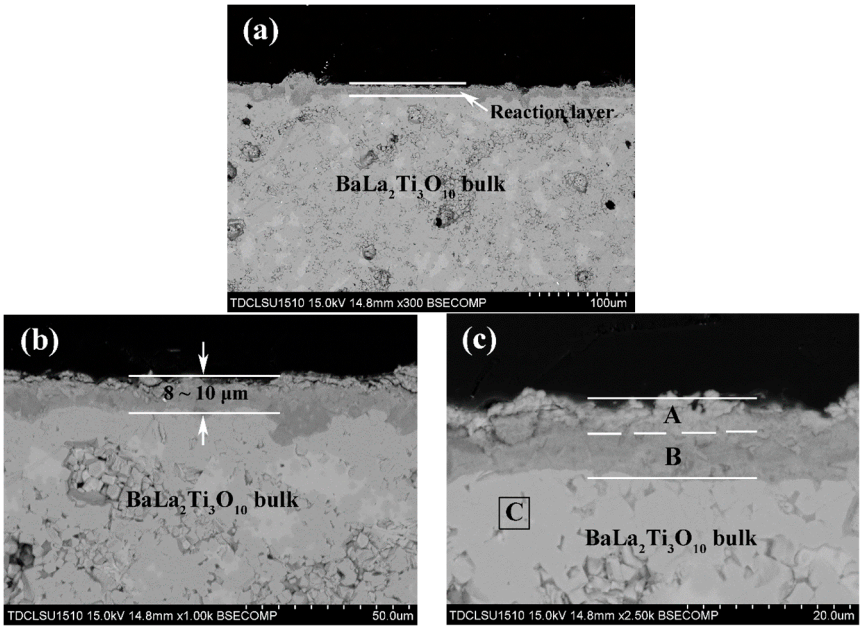

Figure 3. Cross-sectional images of $BaLa_2Ti_3O_{10}$ ceramic after hot corrosion in V_2O_5 salt at 900 °C for 4 h. (**a**–**c**) show the images with different magnifications.

Table 2. Compositions of compounds A–G in Figures 3 and 4 (in at.%).

Corrosion Products	Ba	La	Ti	V	S	O
A	8.17	5.12	8.38	15.29	–	63.04
B	8.95	3.68	7.31	18.17	–	61.89
C	6.31	12.58	20.74	–	–	60.37
D	10.13	6.99	7.53	8.13	9.86	57.36
E	9.34	5.48	7.25	16.46	–	61.47
F	7.18	13.54	20.35	–	–	58.93
G	6.05	13.26	18.78	–	–	61.91

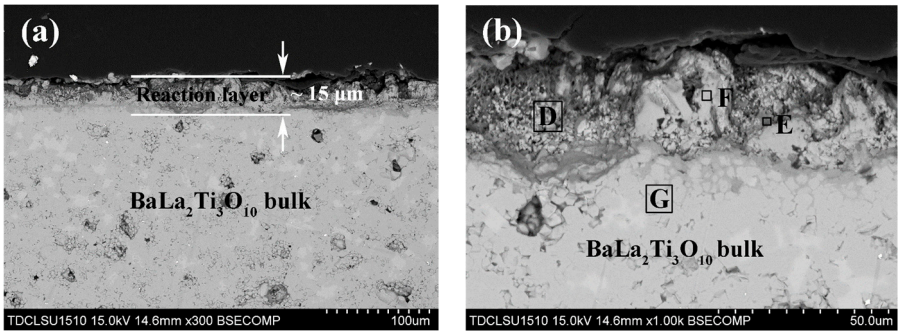

Figure 4. Cross-sectional images of $BaLa_2Ti_3O_{10}$ ceramic after hot corrosion in Na_2SO_4 + V_2O_5 salt at 900 °C for 4 h. (**a**,**b**) show the images with different magnifications.

Figure 4 shows the cross-sectional image of the $BaLa_2Ti_3O_{10}$ sample after hot corrosion in Na_2SO_4 + V_2O_5 salt at 900 °C for 4 h. Being quite different from the case of V_2O_5 corrosion, the reaction layer resulting from Na_2SO_4 + V_2O_5 corrosion exhibits a porous structure and has a larger thickness (~15 μm). At the bottom of the layer, a continuous, grey-contrasted thin band could be observed. Beneath this band, no molten salt trace could be observed, and the bulk keeps structure integrity, suggesting that the molten salt infiltration has been arrested. Figure 4b shows the reaction layer at a higher magnification. EDS analysis results of regions D–G are presented in Table 2. Region D contains La, Ti, Ba, S, V and O elements. Combining with the above XRD result and the surface SEM analysis, this region is determined to consist of $BaSO_4$, $LaVO_4$ and TiO_2. Region E contains Ba, La, Ti, V and O elements. Regions F and G have a close chemical composition, including Ba, La, Ti and O elements. This suggests that they are $BaLa_2Ti_3O_{10}$ bulk.

Based on the above observations, it could be find that molten salts penetration in $BaLa_2Ti_3O_{10}$ thermal barrier ceramics could be arrested, and the inner regions of the samples are free from the attack by molten salts. The rationale behind this is the formation of a dense layer on the sample surface resulting from the reaction between $BaLa_2Ti_3O_{10}$ and the molten salts. The reaction could be understood in terms of the breakdown of the chemical bonds in the crystal by molten salts attack [17,31]. From the viewpoint of crystallography, $BaLa_2Ti_3O_{10}$ crystal could be seen as a tri-perovskite [$La_2Ti_3O_{10}$] layer separated by a Ba layer along c-axis [30]. Since the Ba insertion layers are poorly bonded, they are easier to be attacked by molten salts compared with [$La_2Ti_3O_{10}$] layers. It is thus possible that Ba-O bonds in $BaLa_2Ti_3O_{10}$ would first break in the presence of the molten salts, resulting in the formation of Ba contained corrosion products. Due to the consumption of Ba, La and Ti are enriched in the crystal, which provides a great chance for the molten salt to destroy La-O and Ti-O bonds. As a result, corrosion products of $LaVO_4$ and TiO_2 are formed.

Note that the reaction layer on the sample surfaces has different thickness and structure in the two molten salts, which may be related to the type of the corrosion products. In the case of V_2O_5 molten slat corrosion, the corrosion products are $Ba_3V_4O_{13}$, $LaVO_4$ and TiO_2, and the reaction could be expressed as follow:

$$3BaLa_2Ti_3O_{10}(s) + 5V_2O_5(l) \rightarrow Ba_3V_4O_{13}(s) + 6LaVO_4(s) + 9TiO_2(s) \quad (1)$$

These reaction products have high melt temperatures and exist as solid states in this study. During the corrosion test, there are two processes, i.e., the penetration of the molten salts into the sample and its reaction with the sample. A reaction layer is formed on the sample surface when the reaction has a higher rate than that of the molten salts penetrating into the porous structure. The reaction layer resulting from V_2O_5 molten slat attack has a dense structure, which could effectively inhibit further penetration of the molten salt. Thus, it is reasonable to accept that V_2O_5 attacked $BaLa_2Ti_3O_{10}$ pellet has a thin reaction layer.

When the mixture of Na_2SO_4 and V_2O_5 salts are presented, they react with each other at high temperatures. At 900 °C, the reaction could be represented by the following expression [32]:

$$Na_2SO_4(l) + V_2O_5(l) \rightarrow 2NaVO_3(l) + SO_3(g) \quad (2)$$

Then, the formed products react with $BaLa_2Ti_3O_{10}$. Note that there may exist another possibility, i.e., V_2O_5 or Na_2SO_4 reacts with $BaLa_2Ti_3O_{10}$ separately before the reaction Equation (2) occurs. We mixed Na_2SO_4 and $BaLa_2Ti_3O_{10}$ powders together at a weight ratio of 1:1, and annealed them at 900 °C for 4 h. XRD measurements were performed on the as-mixed powders and the sample after heat treatment, and the results are shown in Figure 5. In the XRD pattern of the as-mixed powders, only $BaLa_2Ti_3O_{10}$ and Na_2SO_4 phases can be detected. By comparison, one could find that the annealed powders exhibit similar XRD pattern appearance to that of the as-mixed powders, and no peak from $BaSO_4$ could be detected. This indicates that Na_2SO_4 and $BaLa_2Ti_3O_{10}$ do not react with each other at 900 °C.

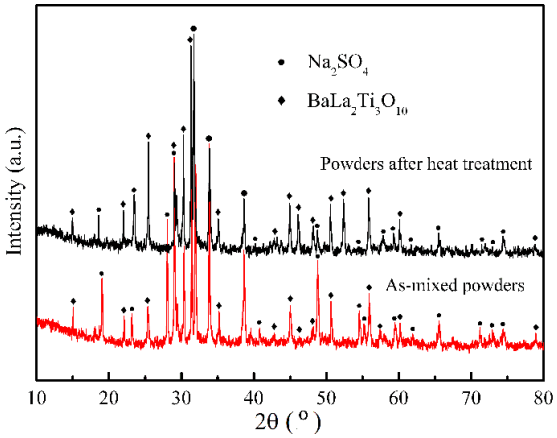

Figure 5. XRD patterns of the as-mixed $BaLa_2Ti_3O_{10}$ and Na_2SO_4 powders and the mixed powders after heat treatment at 900 °C for 4 h.

After the formation of $NaVO_3$ and SO_3, the following reaction could occur:

$$BaLa_2Ti_3O_{10}(s) + 2NaVO_3(l) + SO_3(g) \rightarrow BaSO_4(s) + 2LaVO_4(s) + 3TiO_2(s) + Na_2O(s) \quad (3)$$

It has been reported NaVO3 has better fluidity than V2O5 at liquid state [33–35], thus it has a larger tendency to infiltrate to the sample along cracks/pores, causing the formation a thicker reaction layer, as shown in Figure 4b. Note that the reaction layer on $BaLa_2Ti_3O_{10}$ surface resulting from Na_2SO_4 + V_2O_5 molten slat attack is porous, which could be explained in terms of the participation of SO_3 gas during the reaction process. Some unreacted gas escapes from the bulk, leaving pores and resulting in a decrease in the SO_3 content with the increase of the depth. At a certain depth, no SO_3 exists and only NaVO3 reacts with $BaLa_2Ti_3O_{10}$. The reaction could be described as follow:

$$3BaLa_2Ti_3O_{10}(s) + 10NaVO_3(l) \rightarrow Ba_3V_4O_{13}(s) + 6LaVO_4(s) + 9TiO_2(s) + 5Na_2O(s) \quad (4)$$

This causes the formation of a dense reaction layer, as shown in Figure 4b. The absence of $BaSO_4$ in this layer provides an evidence for this consideration. In the case of Na_2SO_4 + V_2O_5 slat corrosion, the dense reaction layer is formed at a deeper region from the sample surface. Thus, though $BaLa_2Ti_3O_{10}$ TBC candidate has good resistance to Na_2SO_4 + V_2O_5 slat corrosion, it does not perform as good as that in V_2O_5 slat.

4. Conclusions

Hot corrosion behavior of $BaLa_2Ti_3O_{10}$ thermal barrier oxide in V_2O_5 and Na_2SO_4 + V_2O_5 molten salts at 900 °C were investigated. After 4 h corrosion tests, a reaction layer formed on the sample surface, the phase constitution and structure of which depend on the type of the molten salt. In V_2O_5 molten salt, the layer consisted of $LaVO_4$, TiO_2 and $Ba_3V_4O_{13}$, with a dense structure and having a thickness of 8–10 μm. While in Na_2SO_4 + V_2O_5 molten salt, it contained $LaVO_4$, TiO_2 and $BaSO_4$, mainly exhibiting a porous structure, which could be attributed to the participation of SO_3 gas during the formation process of the reaction layer. At the bottom of the porous layer, there existed a dense, thin band, consisting of $Ba_3V_4O_{13}$, $LaVO_4$ and TiO_2. Beneath the dense layer or the band, no molten salt trace existed in the samples, indicating that further infiltration of the molten salts has been arrested. Based on this study, it could be concluded that though $BaLa_2Ti_3O_{10}$ ceramic as TBC candidate has good resistance in both salts, it shows better resistance to V_2O_5 salt corrosion.

Author Contributions: Conceptualization, J.Z.; Methodology, H.L. and J.C.; Validation, H.L. and J.Z.; Formal Analysis, H.L. and J.Z.; Investigation, H.L.; Data Curation, H.L.; Writing—Original Draft Preparation, H.L.; Writing—Review and Editing, J.C. and J.Z.; Supervision, J.Z.

Funding: This research was funded by National Key Research and Development Program (No. 2017YFB1102800), National Natural Science Foundation of China (Nos. 11722219, 11432011, 11620101002).

Conflicts of Interest: The authors declare no conflict of interest.

References

1. Vaßen, R.; Jarligo, M.O.; Steinke, T.; Mack, D.E.; Stöver, D. Overview on advanced thermal barrier coatings. *Surf. Coat. Technol.* **2010**, *205*, 938–942. [CrossRef]
2. Guo, H.; Gong, S.; Zhou, C.; Xu, H. Investigation on hot-fatigue behaviors of gradient thermal barrier coatings by EB-PVD. *Surf. Coat. Technol.* **2001**, *148*, 110–116. [CrossRef]
3. Padture, N.P. Advanced structural ceramics in aerospace propulsion. *Nat. Mater.* **2016**, *15*, 804–809. [CrossRef]
4. Qiao, M.; Zhou, C. Hot corrosion behavior of Co modified NiAl coating on nickel base superalloys. *Corros. Sci.* **2012**, *63*, 239–245. [CrossRef]
5. Zhang, B.Y.; Meng, G.H.; Yang, G.J.; Li, C.X.; Li, C.J. Dependence of scale thickness on the breaking behavior of the initial oxide on plasma spray bond coat surface during vacuum pre-treatment. *Appl. Surf. Sci.* **2017**, *397*, 125–132. [CrossRef]
6. Han, B.; Ma, Y.; Peng, H.; Zheng, L.; Guo, H. Effect of Mo, Ta, and Re on high-temperature oxidation behavior of minor Hf doped β-NiAl alloy. *Corros. Sci.* **2016**, *102*, 222–232. [CrossRef]
7. Guo, H.B.; Vaßen, R.; Stöver, D. Atmospheric plasma sprayed thick thermal barrier coatings with high segmentation crack density. *Surf. Coat. Technol.* **2004**, *186*, 353–363. [CrossRef]
8. Curry, N.; VanEvery, K.; Snyder, T.; Markocsan, N. Thermal conductivity analysis and lifetime testing of suspension plasma-sprayed thermal barrier coatings. *Coatings* **2014**, *4*, 630–650. [CrossRef]
9. Wang, Q.; Guo, L.; Yan, Z.; Ye, F. Phase composition, thermal conductivity, and toughness of TiO_2-doped, Er_2O_3-stabilized ZrO_2 for thermal barrier coating applications. *Coatings* **2018**, *8*, 253. [CrossRef]
10. Xu, Z.H.; Zhou, X.; Wang, K.; Dai, J.W.; He, L.M. Thermal barrier coatings of new rare-earth composite oxide by EB-PVD. *J. Alloy. Compd.* **2014**, *587*, 126–132. [CrossRef]
11. Dong, H.; Han, Y.; Zhou, Y.; Li, X.; Yao, J.T.; Li, Y. The temperature distribution in plasma-sprayed thermal-barrier coatings during crack propagation and coalescence. *Coatings* **2018**, *8*, 311. [CrossRef]
12. Li, C.; Guo, H.; Gao, L.; Wei, L.; Gong, S.; Xu, H. Microstructures of yttria-stabilized zirconia coatings by plasma spray-physical vapor deposition. *J. Therm. Spray Technol.* **2015**, *24*, 534–541. [CrossRef]
13. Gao, L.; Wei, L.; Guo, H.; Gong, S.; Xu, H. Deposition mechanisms of yttria-stabilized zirconia coatings during plasma spray physical vapor deposition. *Ceram. Int.* **2016**, *42*, 5530–5536. [CrossRef]
14. Huang, H.; Liu, C.; Ni, L.; Zhou, C. Evaluation of microstructural evolution of thermal barrier coatings exposed to Na_2SO_4 using impedance spectroscopy. *Corros. Sci.* **2011**, *53*, 1369–1374. [CrossRef]

15. Liu, Z.G.; Ouyang, J.H.; Zhou, Y.; Zhu, R.X. Hot corrosion of V_2O_5-coated $NdMgAl_{11}O_{19}$ ceramic in air at 950 °C. *J. Eur. Ceram. Soc.* **2013**, *33*, 1975–1979. [CrossRef]
16. Li, S.; Liu, Z.G.; Ouyang, J.H. Growth of $YbVO_4$ crystals evolved from hot corrosion reactions of $Yb_2Zr_2O_7$ against V_2O_5 and Na_2SO_4 + V_2O_5. *Appl. Surf. Sci.* **2013**, *276*, 653–659. [CrossRef]
17. Zhou, X.; Xu, Z.; He, L.; Xu, J.; Zou, B.; Cao, X. Hot corrosion behavior of $LaTi_2Al_9O_{19}$ ceramic exposed to vanadium oxide at temperatures of 700–950 °C in air. *Corros. Sci.* **2016**, *104*, 310–318. [CrossRef]
18. Habibi, M.H.; Wang, L.; Liang, J.; Guo, S.M. An investigation on hot corrosion behavior of YSZ-Ta_2O_5 in Na_2SO_4 + V_2O_5 salt at 1100 °C. *Corros. Sci.* **2013**, *75*, 409–414. [CrossRef]
19. Zhong, X.H.; Wang, Y.M.; Xu, Z.H.; Zhang, Y.F.; Zhang, J.F.; Cao, X.Q. Hot-corrosion behaviors of overlay-clad yttria-stabilized zirconia coatings in contact with vanadate-sulfate salts. *J. Eur. Ceram. Soc.* **2010**, *30*, 1401–1408. [CrossRef]
20. Jamali, H.; Mozafarinia, R.; Shoja-Razavi, R.; Ahmadi-Pidani, R. Comparison of hot corrosion behaviors of plasma-sprayed nanostructured and conventional YSZ thermal barrier coatings exposure to molten vanadium pentoxide and sodium sulfate. *J. Eur. Ceram. Soc.* **2014**, *34*, 485–492. [CrossRef]
21. Loghman-Estarki, M.R.; Razavi, R.S.; Edris, H.; Bakhshi, S.R.; Nejati, M.; Jamali, H. Comparison of hot corrosion behavior of nanostructured ScYSZ and YSZ thermal barrier coatings. *Ceram. Int.* **2016**, *42*, 7432–7439. [CrossRef]
22. Loghman-Estarki, M.R.; Razavi, R.S.; Jamali, H. Effect of molten V_2O_5 salt on the corrosion behavior of micro- and nano-structured thermal sprayed SYSZ and YSZ coatings. *Ceram. Int.* **2016**, *42*, 12825–12837. [CrossRef]
23. Nejati, M.; Rahimipour, M.R.; Mobasherpour, I. Evaluation of hot corrosion behavior of CSZ, CSZ/micro Al_2O_3 and CSZ/nano Al_2O_3 plasma sprayed thermal barrier coatings. *Ceram. Int.* **2014**, *40*, 4579–4590. [CrossRef]
24. Liu, H.F.; Xiong, X.; Li, X.B.; Wang, Y.L. Hot corrosion behavior of Sc_2O_3-Y_2O_3-ZrO_2 thermal barrier coatings in presence of Na_2SO_4 + V_2O_5 molten salt. *Corros. Sci.* **2014**, *85*, 87–93. [CrossRef]
25. Liu, Z.G.; Ouyang, J.H.; Zhou, Y.; Xia, X.L. Hot corrosion behavior of V_2O_5-coated $Gd_2Zr_2O_7$ ceramic in air at 700–850 °C. *J. Eur. Ceram. Soc.* **2009**, *29*, 2423–2427. [CrossRef]
26. Guo, L.; Zhang, C.; He, Q.; Yu, J.; Yan, Z.; Ye, F.; Dan, C.; Ji, V. Microstructure evolution and hot corrosion mechanisms of Ba_2REAlO_5 (RE = Yb, Er, Dy) exposed to V_2O_5 + Na_2SO_4 molten salt. *J. Eur. Ceram. Soc.* **2018**, *38*, 3555–3563. [CrossRef]
27. Zhang, C.; Li, M.; Zhang, Y.; Guo, L.; Dong, J.; Ye, F.; Li, L.; Ji, V. Hot corrosion behavior of $(Gd_{0.9}Sc_{0.1})_2Zr_2O_7$ in V_2O_5 molten salt at 700–1000 °C. *Ceram. Int.* **2017**, *43*, 9041–9046. [CrossRef]
28. Guo, L.; Zhang, C.; Li, M.; Sun, W.; Zhang, Z.; Ye, F. Hot corrosion evaluation of Gd_2O_3-Yb_2O_3 co-doped Y_2O_3 stabilized ZrO_2 thermal barrier oxides exposed to Na_2SO_4 + V_2O_5 molten salt. *Ceram. Int.* **2017**, *43*, 2780–2785. [CrossRef]
29. Guo, L.; Zhang, C.; He, Q.; Li, Z.; Yu, J.; Liu, X.; Ye, F. Corrosion products evolution and hot corrosion mechanisms of $REPO_4$ (RE = Gd, Nd, La) in the presence of V_2O_5 + Na_2SO_4 molten salt. *J. Eur. Ceram. Soc.* **2019**, *39*, 1496–1506. [CrossRef]
30. Guo, H.; Zhang, H.; Ma, G.; Gong, S. Thermo-physical and thermal cycling properties of plasma-sprayed $BaLa_2Ti_3O_{10}$ coating as potential thermal barrier materials. *Surf. Coat. Technol.* **2009**, *204*, 691–696. [CrossRef]
31. Chen, X.; Cao, X.; Zou, B.; Gong, J.; Sun, C. Corrosion of lanthanum magnesium hexaaluminate as plasma-sprayed coating and as bulk material when exposed to molten V_2O_5-containing salt. *Corros. Sci.* **2015**, *91*, 185–194. [CrossRef]
32. Habibi, M.H.; Yang, S.; Guo, S.M. Phase stability and hot corrosion behavior of ZrO_2-Ta_2O_5 compound in Na_2SO_4-V_2O_5 mixtures at elevated temperatures. *Ceram. Int.* **2014**, *40*, 4077–4083. [CrossRef]
33. Gitanjaly, H.; Singh, S.; Prakash, S. Role of CeO_2 coating in enhancing high temperature corrosion resistance of Ni-base superalloys as an inhibitor. *Mater. High Temp.* **2010**, *27*, 109–116. [CrossRef]

34. Rocca, E.; Aranda, L.; Moliere, M.; Steinmetz, P. Nickel oxide as a new inhibitor of vanadium-induced hot corrosion of superalloys-comparison to MgO-based inhibitor. *J. Mater. Chem.* **2002**, *12*, 3766–3772. [CrossRef]
35. Ramachandran, C.S.; Balasubramanian, V.; Ananthapadmanabhan, P.V. On the cyclic hot corrosion behavior of atmospheric plasma sprayed lanthanum zirconate based coatings in contact with a mixture of sodium sulphate and vanadate salts: A comparison with the traditional YSZ duplex and NiCrAlY coated samples. *Vacuum* **2013**, *97*, 81–95. [CrossRef]